Acta Materialia 297 (2025) 121365

Contents lists available at ScienceDirect

Acta Materialia

journal homepage: www.elsevier.com/locate/actamat

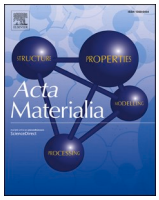

Atomic distribution of alloying elements and second phase particles (SPPs) identification in Optimised ZIRLO

Siyu Huang [a,b], Levi Tegg [a,b], Sima Aminorroaya Yamini [a,b], Lucia Chen [c,d], Patrick Burr [c,d], Jiangtao Qu [a], Limei Yang [a,e], Ingrid McCarroll [a,f], Julie M. Cairney [*,a,b]

[a] Australian Centre for Microscopy and Microanalysis, The University of Sydney, Sydney, 2006, Australia
[b] School of Aerospace, Mechanical and Mechatronic Engineering, The University of Sydney, Sydney, 2006, Australia
[c] School of Mechanical Engineering, University of New South Wales, Sydney, 2052, Australia
[d] UNSW Nuclear Innovation Centre, UNSW Sydney, Kensington, NSW 2052, Australia
[e] School of Civil & Environmental Engineering, University of Technology Sydney, Sydney, 2007, Australia
[f] Max-Planck-Institut für Eisenforschung, Max-Planck-Str. 1, Düsseldorf, 40237, Germany

ARTICLE INFO

Keywords:
Optimised ZIRLO
β-Nb
second phase particle
intermetallic
$Zr(Nb,Fe)_2$
$(Zr,Nb)_3Fe$

ABSTRACT

The accurate chemical composition of second phase particles (SPPs) and solute distributions at grain boundaries and interfaces are still not known for Optimised ZIRLO, with recent debate over the identification of a Zr-Nb-Fe intermetallic phase in these alloys. Here, atom probe tomography (APT) is combined with scanning transmission electron microscopy (STEM), transmission Kikuchi diffraction (TKD), and density functional theory (DFT) to demonstrate that the phase, commonly reported as $Zr(Nb,Fe)_2$, is most likely an intermetallic phase of $(Zr,Nb)_3Fe$ with ~35 at.% Nb.

Interfacial excess is calculated at the β-Nb/α-Zr and $(Zr,Nb)_3Fe$/α-Zr interfaces and at the grain boundaries. Fe is enriched at the interface between β-Nb precipitates and the α-Zr matrix. Fe, Sn, and Nb segregate at α-Zr grain boundaries, no Sn segregation was observed at the interface of β-Nb/α-Zr matrix, and slight Sn segregation was detected at the interface of the intermetallic phases with the α-Zr and at the grain boundaries.

An enhanced understanding of grain boundary segregation, secondary phases composition, and solute behaviour will inform a better understanding of mechanical and corrosion properties, which is expected to be useful for future Zr alloy development.

1. Introduction

Zr alloys are widely used for fuel cladding in nuclear fission reactors [1]. Optimised ZIRLO, first used in 2008 [2], has a composition of 0.8–1.2 Nb, 0.6–0.79 Sn, 0.09–0.13 Fe and 0.09–0.16 O (wt. %) [3]. Sn is highly soluble in α-Zr, while the other alloying elements have limited solubility and form second phase particles (SPPs) [1]. The mechanical properties [1,4,5], corrosion resistance [6,7], and magnetic susceptibility [8,9] of Zr-Nb alloys are strongly influenced by the distribution *Of spps* and solutes in the α-Zr matrix, and on microstructural defects. As such, microanalysis of these microstructural features is beneficial for understanding the behaviour of Zr alloys in nuclear applications.

Alloys of Zr–Nb–Sn with low concentrations of Sn have been shown to display improved corrosion resistance and smaller grain sizes than those with higher concentrations of Sn [10]. The Sn in Optimised ZIRLO and low-Sn ZIRLO is fully dissolved in the α-Zr matrix, so no Sn-rich precipitates are formed [11]. The maximum solubility of Nb in Zr is ~ 0.6 wt. % at the monotectoid transformation temperature; this solubility is reduced significantly by the addition of other solutes such as Sn, Fe, and O [12]. Fe is the main alloying element that enhances the corrosion resistance of Zr alloys for nuclear reactor applications, and this is thought to be through the formation of Fe-containing SPPs [13]. Fe and Nb are both β-Zr stabilizers and they combine to form various types o.ff SPPs [12]. SPPs composition, size and distribution directly affect the corrosion behaviour and formation of hydrides in the matrix by changing the solute concentrations in the matrix and by causing nodular corrosion in areas where large particles precipitate [12]. These factors change the electrochemical behaviour of the oxide barrier layer on the metal surface [14], which in turn, influences the diffusion of oxygen and hydrogen across the barrier layer [15,16].

* Corresponding author.
E-mail address: julie.cairney@sydney.edu.au (J.M. Cairney).

https://doi.org/10.1016/j.actamat.2025.121365
Received 3 March 2025; Received in revised form 9 July 2025; Accepted 19 July 2025
Available online 20 July 2025

An index has been introduced to predict the composition and type o. ff SPPs formed in Zr–Sn–Nb–Fe alloys according their nominal composition [12]. This index suggests that body-centred cubic (BCC) β-Nb and Laves phase are expected to form in Optimised ZIRLO. Intermetallic phases of cubic $Fd\bar{3}m$, Ti_2Ni type (C15) [17,18] and hexagonal P63/mmc, $MgZn_2$ type (C14) [17–19] are reported to form with β-Nb in Zr-Nb-Fe alloys. Researchers agree on the identification of cubic C15, $(Zr,Nb)_2Fe$, Laves phase in which Nb atoms randomly occupy the atomic sites of Zr in the lattice structure of Zr_2Fe. Although Zr_2Fe is a stable phase at high temperature (above 775℃) in the binary Zr-Fe system [20], its characteristically low Nb content (~10 % Nb, ~30 % Fe, ~60 % Zr) and cubic crystal structure leaves no ambiguity in identification of this phase in the ternary Zr-Nb-Fe alloys [21]. However, there is debate in the literature over the correct identification of the hexagonal C14 Zr $(Nb,Fe)_2$ phase, in which Nb replaces Fe atoms in a $ZrFe_2$ phase with a hexagonal crystal structure. This intermetallic phase, $Zr(Nb,Fe)_2$, is believed to improve the radiation resistance of Optimised ZIRLO compared to Zircaloy-4 [22]. The transfer of Fe from precipitates to the matrix under irradiation strengthens the alloy [23] and radiation-induced defects can sink at the interface of precipitates with the matrix, reducing the defect density [24] and stabilising the microstructure [12]. The hexagonal $ZrFe_2$ is a high-temperature stable phase which forms at liquidus temperatures (at temperatures as high as 1673℃) in Zr-Fe alloys with <76 at. % Zr and remains stable at temperatures down to 780℃, however, it is stable at temperatures below 780℃ in Fe alloys with <35 at. % Zr [20]. On the other hand, a low temperature stable orthorhombic Zr_3Fe phase forms through a peritectoid transformation of Zr_2Fe at 851℃ in Zr-rich binary alloys [20]. A detailed review [21] on the reported hexagonal $Zr(Nb,Fe)_2$ phase shows that the majority of compositions reported for this phase fit well with a low temperature stable phase of $(Zr,Nb)_3Fe$ with a similar crystal structure. Although those authors [21] do not rule out the formation of $Zr(Nb,Fe)_2$ phase in Zr alloys due to heat treatment of Zr alloys at high temperatures, the low Nb diffusion in Zr and non-equilibrium conditions of commercial alloys, they have provided evidence for misidentification of this phase in the literature. Due to the very small size (<100 nm) of particles that are embedded in the matrix, compositional data collected from energy dispersive spectroscopy (EDS) analysis can be subject to interference of signals from the matrix composition during transmission electron microscopy (TEM) investigations.

To resolve this debate for Optimised ZIRLO, we have used atom probe tomography (APT) to accurately measure the chemical composition *O. spps*, and to determine the solute distribution in the Zr matrix, at grain boundaries, and *At spp* interfaces. This is combined with aberration-corrected scanning transmission electron microscopy (STEM), EDS, and transmission Kikuchi diffraction (TKD) analyses to realise the segregation width and elemental distribution at α-Zr grain boundaries and microstructural features. The experimental results are then correlated to thermodynamics information obtained from density functional theory (DFT) calculations of ternary disordered intermetallics in the Zr-Fe-Nb phase space.

2. Methods

Optimised ZIRLO samples were obtained from Westinghouse Electric AB with nominal composition of 0.8–1.2 Nb, 0.6–0.79 Sn, 0.09–0.13 Fe and 0.09–0.16 O (wt %) [3]. Cladding tubes of 9.5 mm in outer diameter and 0.65 mm in thickness were cut to 15 mm in length, then sectioned into matchsticks of 0.4 × 0.4 × 15 mm. The atom probe specimens were prepared by electropolishing in two stages: first at 12 V DC in 25 % perchloric acid in glacial acetic acid, then at 5–7 V DC in 2 % perchloric acid in 50 % 2-butoxyethanol and 50 % methanol using the micro-loop method [25]. The specimens were then rinsed in methanol and swiftly transported to the focused ion-beam microscope in air, or directly to the atom probe microscope submerged in methanol until they were ready to be loaded into the instrument. For some specimens, a Zeiss Auriga focused Ga-ion beam (FIB) or a ThermoFisher Helios G4 plasma focused ion beam (PFIB) was used to perform annular milling to remove the anodic film or oxide layer. A final 5 kV cleaning process was performed to remove any Ga or Xe damage during milling process. The removal of surface oxide by FIB milling improved the yield in the atom probe. A previous study showed evidence of the formation of Zr hydrides in samples prepared by plasma FIB at room temperature instead of under cryogenic conditions; however, the aim of the current study is to determine the accurate chemical composition *O. spps*, which is not affected by the potential formation of hydrides.

APT was performed using a Cameca LEAP4000X Si and a Cameca Invizo 6000, both operated in laser-pulsed mode. For data collected on the Invizo 6000, a base temperature of 50 K, laser pulse energy of 800 pJ, pulse repetition rate of 200 kHz, and a target detection rate of 2 % were used. For data collected from the LEAP4000X Si, a base temperature of 50 K, laser pulse energy of 100 pJ, pulse repetition rate of 200 kHz, and a target detection rate of 0.5 % were used. Data was reconstructed and analyzed using Cameca's Visualization and Analysis Software (AP Suite 6). The average evaporation field was set for Zr (28 V/nm), and the detector efficiency was set to 0.57 for the LEAP4000X Si and 0.62 for Invizo 6000. For the LEAP4000X Si data, the AP Suite 6 default image compression factor and field factor were used. For the Invizo 6000, the image compression factor and the field factor were determined to ensure the observed microstructural features had geometry consistent with that observed using electron microscopy [25]. Several atom probe specimens were analysed to capture various microstructural features, to determine the chemical composition of β-Nb, Zr-Nb-Fe intermetallic phases, and to measure the segregation of alloying elements to grain boundaries in this alloy. For ease of comparison between figures, β-Nb precipitates are labelled N*x* ($x = 1$ to 4), intermetallic precipitates are labelled P*y* ($y = 1$ to 4), and grain boundaries are labelled GB*z* ($z = 1$ to 3) throughout the text. Interfacial excess calculations were performed by fitting curves to the cumulative ion count profiles (also known as "ladder plots"), with the uncertainty determined from the sum of the cumulative measurement uncertainty and the uncertainty in the constant solute content of each grain [26]. A few peak overlaps were observed in these mass spectra. In all cases, one peak had 50–100 times greater magnitude, confirming that the effect of peak overlap on compositional accuracy is small. These include ^{93}Nb overlap with ^{92}ZrH, where the Nb peak height far exceeds that of the ZrH peaks for the + and ++ charge states, particularly inside the Laves phases where ZrH content was nearly zero; $^{56}Fe^{+}$ overlaps with $^{96}ZrO^{++}$, but the Fe peak height far exceeds the ZrO^{++} peak height for that isotope. The majority of the ZrO counts come from the $^{90–94}ZrO$ peaks, which constitute 97 % of its counts; $^{112}Sn^{++}$ and $^{114}Sn^{++}$ overlap with $^{56}Fe^{+}$ and $^{57}Fe^{+}$, but the Fe peak height far exceeds the Sn peak height for those isotopes. The majority of the Sn counts come from the $^{115–124}Sn$ peaks, which constitute 98 % of the natural abundance. Peak overlap is more significant for specimens containing high H or D, complicating the interpretation of the ZrH_x^n peaks. Compositional analysis of intermetallic and Nb precipitates are largely unaffected.

TEM lamellae were prepared using a plasma focused ion beam (PFIB) according to conventional lift-out procedures [27] using a copper half-grid. A final 5 kV clean was performed to remove potential Xe damage. High-angle annular dark-field (HAADF) STEM images were collected on a ThermoFisher Themis Z equipped with a double spherical aberration corrector operated at 300 kV. EDS was performed to determine elemental composition at the near-atomic scale, and valence electron energy loss spectroscopy (EELS) was also performed to determine the phase composition of the sample.

For transmission Kikuchi diffraction (TKD) analysis, a 5 mm × 5 mm sample was cut from the as-received cladding, mechanically polished to ~30–50 μm thick using a MultiPrep polishing system, and then milled using the Gatan precision ion polishing II (PIPS II) system under cryogenic conditions. Samples were cleaned by using 0.2 keV Ar ion beam

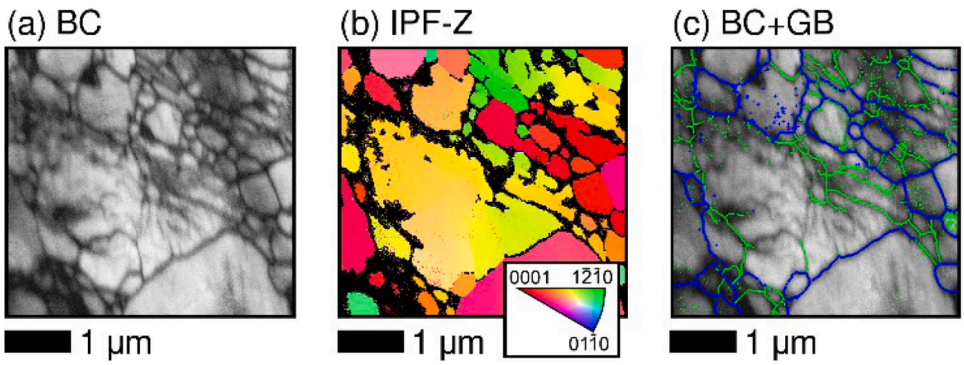

Fig. 1. (a) Band contrast (BC) map; (b) TKD inverse pole figure (IPF) Z map; (c) TKD local misorientation map of Optimised ZIRLO lamella overlaid on BC map, subgrain angle was set as 2°, with green and blue colours show grain boundaries misorientation angles of 2–15° and >15°, respectively.

across $a \pm 5°$ angle range before analysis. TKD was carried out in a Zeiss ULTRA Plus scanning electron microscope (SEM), operating at 30 kV and a step size of 7 nm. The TKD data was analysed using Oxford Instruments' HKL Tango software and cleaned with wild spikes and 5 nearest neighbours once.

DFT calculation was performed to aid the structural identification of the Zr-Nb-Fe intermetallic phases. We considered the energy required for phase decomposition and phase transformation between $Zr(Fe,Nb)_2$, $(Zr,Nb)_3Fe$ and $(Zr,Nb)_2Fe$, and their binary counterparts. As a first order approximation, we only considered ground state enthalpy, and disregarded any entropic and temperature effects, or contributions from interfacial energy and strain. We have also estimated an upper bound of the configurational entropy, which is expected to be the strongest entropic contribution. We do not perform full thermodynamic treatment of all contributions to the free energy, because insufficient information is available about the interface of the observed precipitates in questions to enable accurate calculation of interfacial and strain energy. The maximal configurational entropy, S^{max}, was calculated using Boltzmann statistics:

$$S^{max} = -k_B \ln\left(\frac{N!}{\prod_i N_i!}\right) \quad (1)$$

where k_B is Boltzmann constant, N is total atomic sites and N_i are the those occupied by species i. This treatment neglects statistical correlations, i.e. it implicitly assumes that the system behaves like an ideal mixture, and therefore the true configurational entropy of a real solid solution must be lower than this estimate. All reaction energies are reported in eV per formula unit (f.u.) of reactant and represent the ground state enthalpy unless otherwise stated. Disorder was modelled in the relevant sublattice by creating special quasi-random structures (SQS), in supercells comprising 144 atoms ($(Zr,Nb)_2Fe$) or 192 atoms ($(Zr,Nb)_3Fe$ and $Zr(Fe,Nb)_2$). SQS cells were generated using the MCSQS code [28], with pair, triplet, and quadruplet correlations defined up to the fifth, third, and first nearest neighbours, respectively. For each structure, the atomic positions and lattice parameters were relaxed using the Vienna Ab-initio Simulation Package (VASP) [29], until the energy difference converged below $\pm 10^{-6}$ eV. The Brillouin zone of the supercells was sampled with a $3 \times 3 \times 3$ k-point mesh centred on the Γ point. The Zr, Nb and Fe species were modelled with projector augmented wave pseudopotentials with 12, 13, and 14 valence electrons, respectively, a cut-off energy of 350 eV, and band-smearing of 0.1 eV using first order Methfessel-Paxton scheme.

3. Results and discussion

3.1. Overview of microstructure

Fig. 1(a) shows a band contrast (BC) map obtained using TKD. Fig. 1 (b) shows an inverse pole figure (IPF) image in the Z direction, and Fig. 1 (c) shows BC overlaid with low-angle grain boundaries (LAGBs) with misorientation angles from 2–15° in green, and high-angle grain boundaries (HAGBs) with misorientation angles greater than 15° in blue. These results show that this region of the sample consists of fine grains of 0.2 to 2 μm in size with a combination of low and high-angle grain boundaries. No hydrides were identified through phase mapping, confirming that the cryogenic temperature used during Ar-ion milling successfully prevented their formation [30].

Fig. 2(a) shows a HAADF STEM image of the Optimised ZIRLO specimen, showing the various second phase particles. By correlating STEM HAADF images and EDS mapping (Figs. 2(b) and (c)), we identify three distinct phases in the α-Zr matrix.

(a) Precipitates with light contrast in the HAADF image that have a high concentration of Nb; EDS mapping of the area 1 in Fig. 2(a), also shown at higher magnification in Figs. 2(d) to (F) shows that these regions are enriched in Nb only. This suggests they are β-Nb.
(b) A darker contrast phase that still appears lighter than the matrix, containing both Fe and Nb; EDS mapping of area 2 in Fig. 2(a), shown in higher magnification in Figs. 2(g) to (i) support formation of an intermetallic phase containing Fe and Nb. This suggests they are Zr-Nb-Fe intermetallic precipitates with an irregular geometry, contrasting with the β-Nb which are generally smaller and approximately spherical.
(c) A dark elongated phase, larger than previous particles, with no solutes detected by EDS. This phase is assumed to be Zr hydride. δ- ZrH_{2-x}, which appear darker than the matrix [30] under HAADF imaging, have previously been observed in samples prepared by plasma FIB at room temperature instead of under cryogenic conditions [30]. The identity of the hydride phase in our sample was confirmed by using valence electron energy loss spectroscopy (EELS) measurements presented in the Supporting Information (Fig. S1) [31].

Fig. 2 (j to l) show atomic-resolution STEM-HAADF images of three phases observed in this material together with relevant two-dimensional fast Fourier transforms of the images, used to determine the crystal orientations. Fig. 2(j) shows hexagonal close packed (HCP) α-Zr phase viewed along $[\bar{1}10]$; Fig. 2(k) demonstrate body centred cubic (BCC) β-Nb phase viewed along $[\bar{1}11]$; and Fig. 2(l) shows the intermetallic Zr-Nb-Fe phase shown in Fig. 2(i). The crystal orientation of the intermetallic, the spots on the FFT image of this phase were indexed to an orthorhombic crystal structure with Cmcm space group.

3.2. β-Nb precipitates

Formation of a β-Nb phase is frequently reported in commercial Nb-

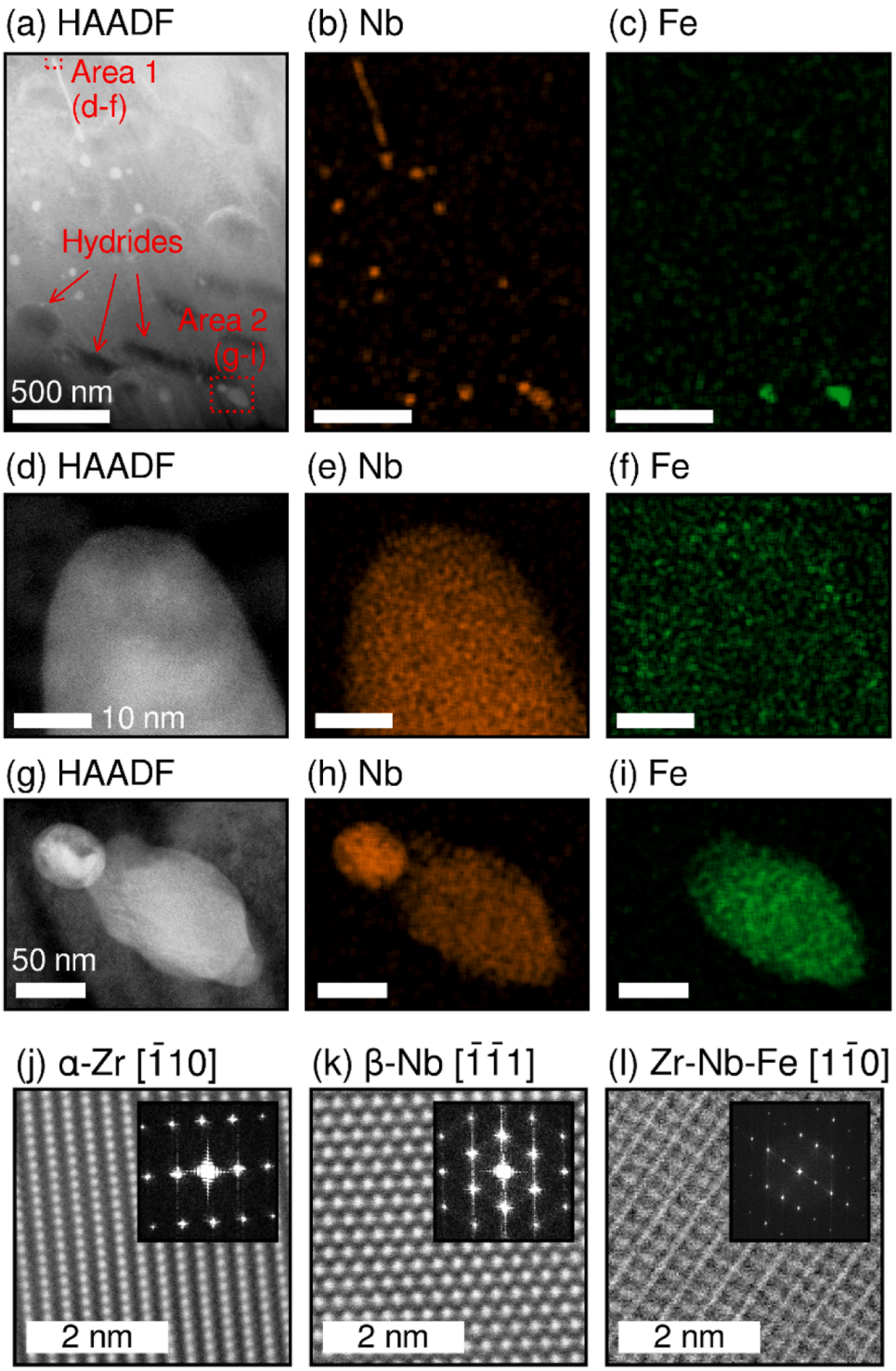

Fig. 2. (a) STEM HAADF image of Optimised ZIRLO, hydrides are annotated in the figure; (b) and (c) are EDS maps of Fe and Nb in Fig. 2(a) respectively; (d) STEM HAADF image of the feature of interest annotated as Area 1 in Fig. 2(a); (e) and (f) are EDS maps of Fe and Nb in Fig. 2(d) respectively, showing β-Nb phase; (g) STEM HAADF image of the Area 2 in Fig. 2(a); (h) and (i) are EDS maps of Fe and Nb in Fig. 2(g) respectively, showing both β-Nb and intermetallic phases. Atomic resolution STEM-HAADF images of (j) hexagonal close packed (HCP) α-Zr viewed along $[\bar{1}10]$, (k) BCC, β-Nb viewed along $[\bar{1}11]$, and (l) a Zr-Nb-Fe intermetallic phase, indexed to the Cmcm space group of an orthorhombic structure, viewed along $[1\bar{1}0]$. Inset axes show two dimensional fast Fourier transforms of the images, used to determine crystal orientation. The STEM image in (l) is the same intermetallic particle analysed in Fig. 2(i).

added Zr alloys that are heat treated below their monotectoid transformation. Precipitates of this phase are reported to contain over 80 % Nb and no Fe [32–34]. These precipitates have been analysed by EDS; and considering the small size of β-Nb phase (~ 50 nm) and the thickness of the TEM lamella, the uncertainty of measured values from the curved interfaces between the precipitates and the Zr matrix are anticipated to be high for elements with low concentrations. Additionally, artefacts caused by the X-ray signal of Fe scattered from the pole-piece in the TEM may also interfere with the measured concentration of Fe [21].

Fig. 3 shows an atom probe reconstruction collected using the Invizo

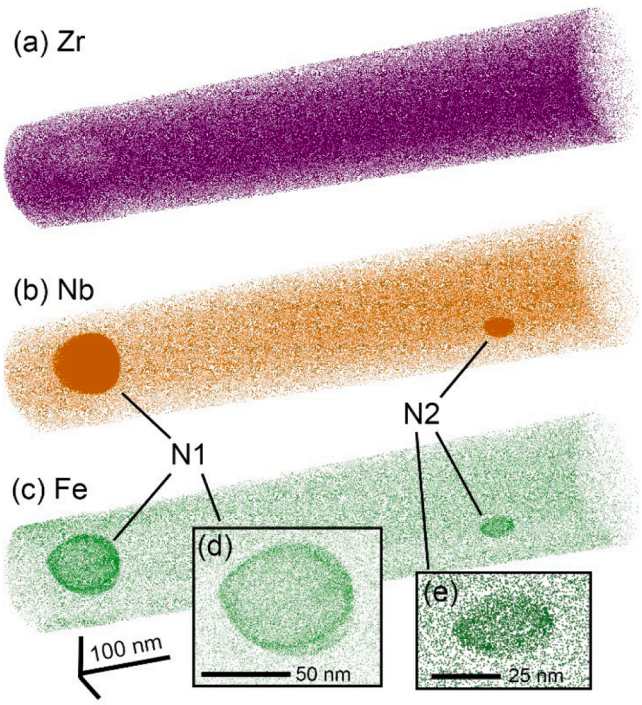

Fig. 3. Atom probe reconstructed volume showing (a) Zr; (b) Nb; (c) Fe ion distribution, collected using the Invizo 6000, (d) and (e) close-ups of the N1 and N2 precipitate, respectively, showing Fe decorates the interface between the β-Nb and the α-Zr matrix. Fe is rendered with spheres in (e) to enhance visibility.

6000 from an electropolished sample, including two β-Nb precipitates, labelled N1 and N2. A Nb 40 at. % isoconcentration surface (isosurface) was used to define a region of interest (ROI) to determine the composition of these precipitates (and two others, presented in Figure S3 of the supporting Information), summarised in Table 1. The results show that β-Nb precipitates contain 81–90 % Nb, very low concentrations of Fe and Sn alloying elements, and varying Zr. No correlation was proved between the size and Nb content of β-Nb precipitates, however, the smaller the precipitate, there is larger uncertainty in determining its core composition. The variation in Nb content of β-Nb precipitates might result from factors such as precipitate geometry or proximity to grain boundaries or other precipitates. With only four β-Nb precipitates observed (and only two fully contained in the analysis volume), we are unable to confidently comment on the mechanism behind the varying Nb content between β-Nb. Precipitates N1, N3 and N4 are fairly large, suggesting the measurements from their core are not strongly affected by atom probe trajectory aberrations. Proximity histograms (proxigrams), normal to the interface of these precipitates with α-Zr, were used to calculate composition profiles for all β-Nb precipitates [25]. The profiles for Zr, Nb and Fe are shown in Fig. 4. Fig. 3(d) is a close-up of the N1 precipitate shown in Figs. 3(b) and (c), with Fe ions shown as green spheres. Fig. 3(d) and Fig. 4(b) show that Fe atoms segregate at the interface between the α-Zr matrix and β-Nb precipitates, similar to previous reports [35,36]. Peak measured concentrations of segregated Fe at the interface of α-Zr with β-Nb precipitates vary between ~0.5 to ~1.2 at. %.

Noting that peak concentrations can be affected by trajectory aberrations [25], Fe segregation was quantified using the Gibbsian boundary excess (Γ_i), at the interfaces of the β-Nb precipitates and the α-Zr matrix. Γ_i is the number of excess atoms per unit area of a boundary, defined as:

$$\Gamma_i = \frac{N_{excess}}{e_d A} \tag{2}$$

where N_{excess} is the number of excess ions (here i = Fe), A represents the surface area of the region-of-interest and e_d denotes the efficiency of the atom probe detector. The values of e_d are 0.57 and 0.62 for data collected from LEAP 4000X Si and Invizo 6000 data, respectively [37]. N_{excess} and Γ_{Fe} were measured calculated for several β-Nb precipitates and are presented in Table 2. These N_{excess} were found by fitting cumulative density function of the sum of a constant and Gaussian curve to

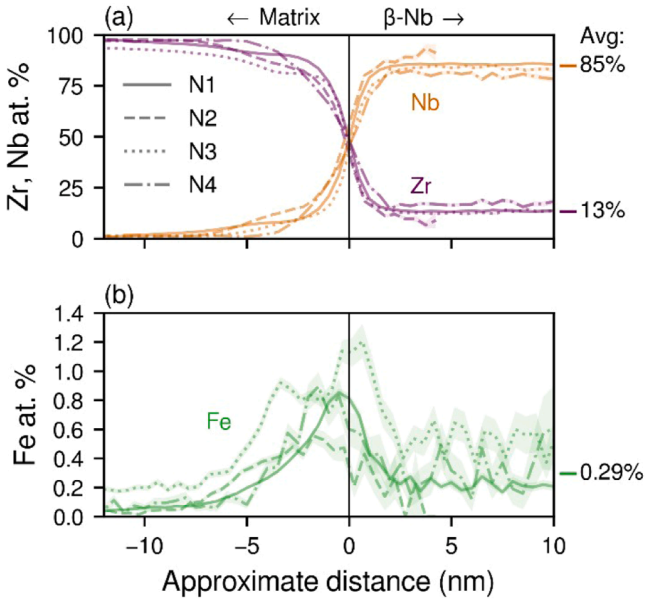

Fig. 4. Composition profiles between the matrix and the β-Nb for (a) Nb and Zr; (b) Fe, four different particles (N1 to N4).

Table 2
The average Fe fractional monolayer coverage for the four β-Nb precipitates described in this work. The parenthesised numbers indicate the standard deviation. The values for N1 and N2 were calculated from a proxigram over an Nb isosurface, whereas N3 and N4 were from a 1D concentration profile over a cylindrical RO1 because they extended beyond the edge of the reconstruction. The uncertainty is propagated from the uncertainty in the Fe measurement [26].

	N1	N2	N3	N4
N_{Fe} (atoms)	12,533 ± 860	2699 ± 333	905 ± 216	543 ± 157
Γ_{Fe} (atoms/nm^2)	2.3 ± 0.2	4.7 ± 0.6	1.6 ± 0.4	2.1 ± 0.6
ϕ_{Fe} (fractional monolayer)	0.17 ± 0.01	0.34 ± 0.04	0.11 ± 0.03	0.15 ± 0.04

Table 1
Bulk composition of the four β-Nb precipitates described in this work. The estimated standard deviations are parenthesized, e.g. 13.33(5) = 13.33 ± 0.05. These calculations include ions contained within a Nb 40 at. % isosurface. This calculation excludes C, O, N and H.

	Zr	Nb	Fe	Cr	Sn	Ti	Al	Mn	V
N1	13.33(5)	86.3(2)	0.224(6)	0.022(2)	0.078(3)	0.005(1)	0.008(1)	–	–
N2	10.2(6)	90(2)	0.13(7)	–	0.13(7)	–	–	–	–
N3	14.0(1)	84.9(4)	0.57(3)	0.24(2)	0.19(2)	0.011(3)	–	0.001(1)	0.061(8)
N4	18.3(2)	81.0(5)	0.42(3)	0.18(2)	0.15(2)	–	–	–	0.037(8)

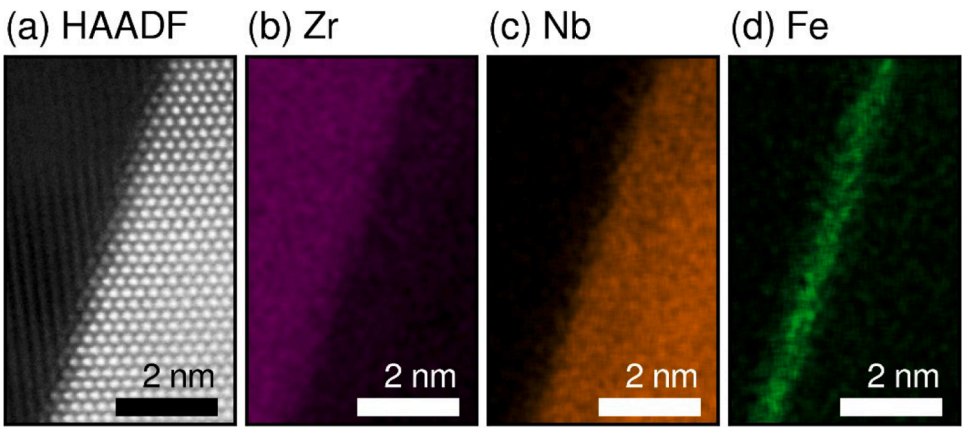

Fig. 5. STEM analysis of the interface between α-Zr matrix and β-Nb precipitate, (a) HAADF image; EDS map of (b) Zr, (c) Nb, (d) Fe.

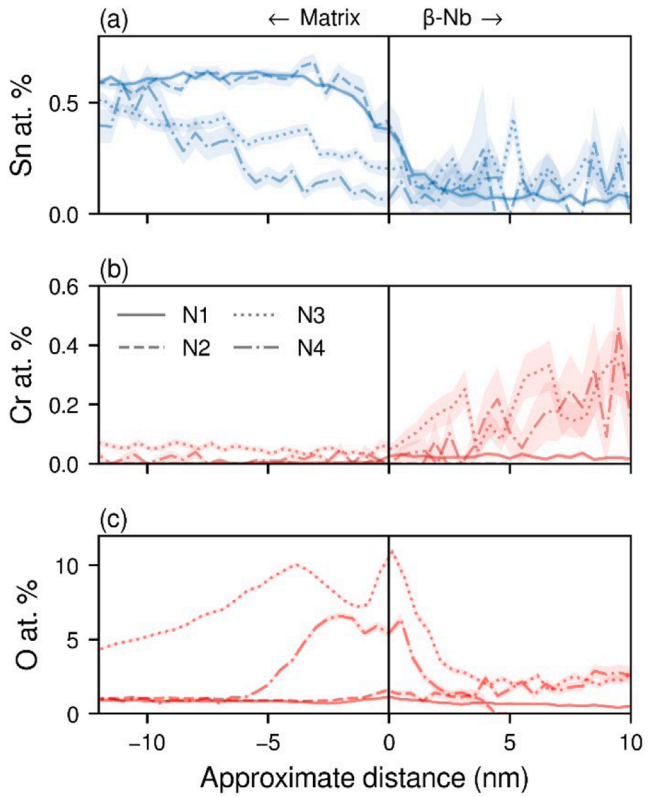

Fig. 6. One dimensional concentration profile of (a) Sn; (b) Cr; and (c) O, across ROIs normal to the α-Zr / β-Nb interfaces shown for N1 to N4. The shaded area around the curves refers to the uncertainty of the calculated values of concentrations.

the ladder plots of Fe content across this interface [26]. The Gibbsian interfacial excess can be compared with measurements made using other methods by converting it into an equivalent solute coverage on the interface. A solute's fractional monolayer coverage, denoted as ϕ_i, can be approximated using the following equation:

$$\phi_i = \frac{\Gamma_i}{\rho\omega} = \frac{N_{\text{excess}}}{\rho\omega e_d A} \tag{3}$$

where $\rho = 43$ atom/nm^3 is the atomic density of Zr and $\omega = \omega_{[0001]} = 0.323$ nm is the plane spacing for the α-Zr [0001] direction [38,39]. The fractional monolayer coverage of Fe for four β-Nb precipitates identified in this study are also shown in Table 2.

A previous HAADF STEM and EDS study of a low-Sn ZIRLO alloy reported a concentration of 6.3 wt. % (~ 9.85 at. %) Fe at the interface around a ~ 70 nm β-Nb precipitate, compared to 1 wt. % Fe in the matrix [36]. This is much higher than the values measured in the current study for β-Nb precipitates ranging from 10 to >100 nm, suggesting that the Fe X-ray signal from the TEM pole piece contributed to the reported Fe concentrations determined by the EDS technique in the previous report. We find that the concentration of Fe is consistently higher in the β-Nb precipitates than in the α-Zr matrix (Fig. 4(b)), in agreement with much higher solubility of Fe in Nb relative to Zr [11]. The datasets presented in Fig. 4 have not been spatially calibrated, however, the measured thickness of the Fe segregated layer is estimated to be <3 nm, considering some widening of the measured interfacial thickness due to the local magnification effects or misalignment of the ROI with the normal to the interface [25]. To accurately estimate the thickness of the segregated Fe layer at the interface between the α-Zr and the β-Nb, the interface was analysed by STEM EDS [40]. Fig. 5 shows a HAADF image and an EDS map of Zr, Nb, and Fe, at the interface of α-Zr matrix with the β-Nb precipitates, indicating that the thickness of the segregated Fe layer is <1 nm. Previous studies have shown that this segregation is greatly reduced or even entirely absent after neutron irradiation of 18 dpa [36], most likely due to the increased concentration of irradiation-induced defects and amorphization of precipitates [41].

Fig. 6 shows the one-dimensional compositional profile of Sn, Cr, and O elements across cylindrical ROIs normal to the interfaces of α-Zr matrix with β-Nb precipitates N1 to N4, determined from APT. Carefully-placed ROIs were used for these measurements to avoid explicitly including the surface oxide in the composition profile; an isosurface over Nb would capture both the surface oxide and the matrix, complicating interpretation of oxygen content in the matrix. The concentration of Sn in the matrix is much higher than in the precipitates, and no Sn segregation is observed at the interfaces. Cr, a residual/impurity element in Optimised ZIRLO, is detected within the β-Nb precipitates (Fig. 6). The oxygen profile varies between samples. Oxygen interstitially dissolves in Zr alloys at reasonably high concentrations [42]. Optimised ZIRLO contains oxygen that is dissolved in the matrix and at precipitates. Zr alloys oxidise easily and some of precipitates analysed in this study were close to the sample surface, where major oxidation occurred either due to atmospheric corrosion or during electropolishing. We therefore expect that the amount of oxygen detected by APT is unrelated to the oxygen content of the original sample. We have found oxygen in solution in Zr and SPPs at concentrations as high as a few percentage (between 0.6–10.0 at. %), with no sign of oxide particles, consistent with the high solubility of oxygen of ~28 at. % in α-Zr [43].

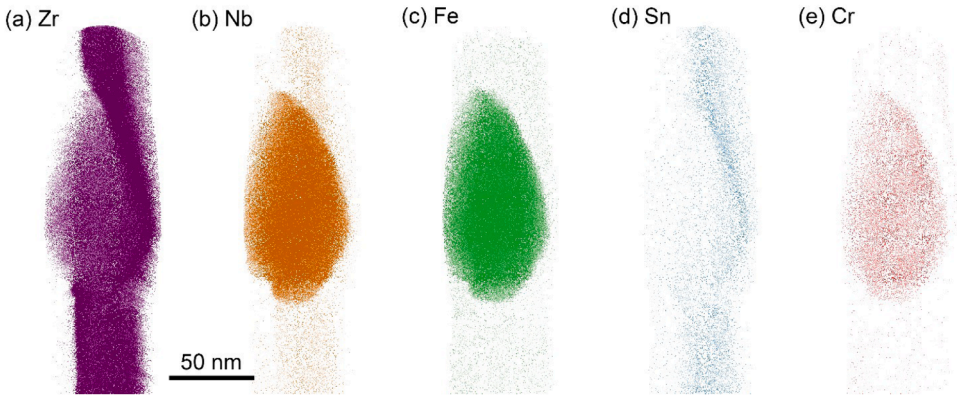

Fig. 7. Reconstructed positions of (a) Zr, (b) Nb, (c) Fe, (d) Sn and (e) Cr for a dataset containing an intermetallic phase, labelled P3 in this study. This data was obtained from Invizo 6000.

Table 3
Measured composition of the three intermetallic phases described in this work. These calculations include ions contained within a (Nb,Fe) 40 at. % isosurface. The standard deviations are indicated in parentheses, e.g. 40.1(1) = 40.1 ± 0.1.

	Zr	Nb	Fe	Sn	Cr	Mn	Ti	V
P1	40.1(1)	35.54(9)	22.85(7)	0.152(5)	1.25(1)	0.013(1)	0.016(2)	0.038(3)
P2	38.92(5)	30.46(4)	29.04(4)	0.071(2)	1.388(8)	0.0100(6)	0.0166(8)	0.027(1)
P3	39.12(3)	36.86(3)	23.03(2)	0.098(1)	0.851(4)	0.0196(6)	0.0136(5)	0.0113(4)

Table 4
The relative (Zr+Nb)/3, (Nb+Fe)/2, Zr and Fe contents of the three intermetallic precipitates described in this work. These compositions were obtained by normalising composition to Zr + Nb + Fe = 100 at %, excluding all other elements.

	(Zr + Nb)/3	Fe	Zr	(Nb + Fe)/2
P1	25.60(6)	23.19(7)	40.7(1)	29.63(8)
P2	23.50(3)	29.49(4)	39.58(5)	30.21(4)
P3	25.58(2)	23.26(2)	39.51(3)	30.24(3)

3.3. Zr-Nb-Fe intermetallic phases

The reconstruction in Fig. 7 shows the distribution of Zr, Nb, Fe, Sn, and Cr atoms in a specimen that contains an intermetallic phase, ~100 nm in size, consisting of Nb, Fe and Cr. This precipitate is labelled P3. Sn is dissolved in the α-Zr matrix and segregates to the interface between the intermetallic phase and the matrix. The Cr, which has extremely low solubility in Zr alloys [44], is heavily segregated to the SPP. A tendency toward solute segregation is inversely related to bulk solubility [45], so any Cr would be expected to be incorporated in SPPs and segregate to microstructural features such as grain boundaries in Zr alloys [46,47].

The APT specimens analysed in this study contained 3 intermetallic phases with compositions similar to the one shown in Fig. 7, designated P1 to P3. Atom probe reconstructed position of atoms for P1 and P2 are presented in the Figures S4 and S5 of the Supporting Information. The compositions, calculated by considering ions within a 40 % (Nb, Fe) isosurface, are summarised in Table 3. These intermetallic phases contain ~ 35 % Nb and 25 % Fe, corresponding to the chemical composition of hexagonal $Zr(Nb,Fe)_2$ Laves phase in the literature [19,21]. However, as described in the introduction, there is some debate over the correct identification of this phase, and hexagonal $(Zr,Nb)_3Fe$ has the potential to be misidentified as hexagonal $Zr(Nb,Fe)_2$ Laves phase. To address this concern, we look at the ratios of different species to identify the phase. If the precipitates are $(Zr,Nb)_3Fe$, the values of (Zr+Nb)/3 should be equivalent to the Fe content. If the precipitates are $Zr(Nb,Fe)_2$, the values of (Fe+Nb)/2 should be equivalent to the Zr content. Table 4 reveals a much better match for $(Zr,Nb)_3Fe$, and a poor match for $Zr(Nb,Fe)_2$, suggesting that this phase observed here is $(Zr,Nb)_3Fe$, and supporting the idea that this phase may have previously been misidentified [48]. Further evidence in support of the $(Zr,Nb)_3Fe$ phase comes from a simple stoichiometry argument that mathematically, $Zr(Nb,Fe)_2$ can only accommodate 33 at. % Zr. In order for this structure to potentially accommodate ~40 % Zr, as measured in P1-P3 (Table 3), some Zr atoms would have substituted the Fe sublattice, i.e. $Zr(Zr,Nb,Fe)_2$, which is shown to be highly unlikely in the DFT calculation described in the following section.

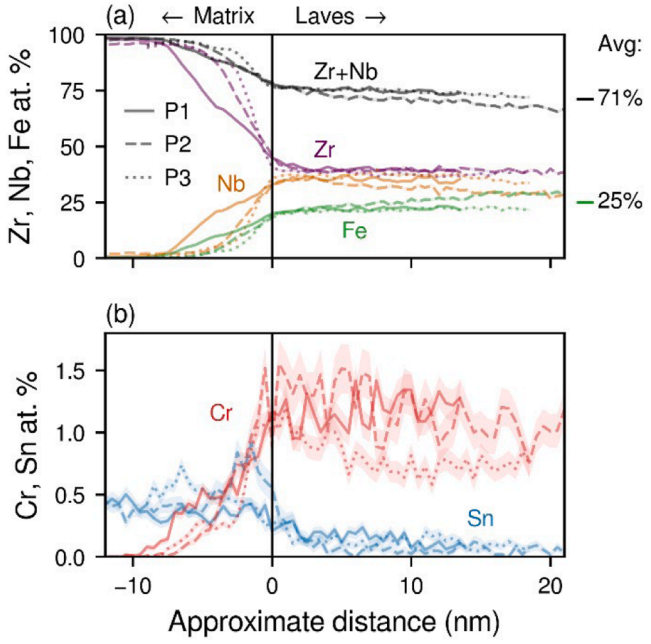

Fig. 8. Composition profiles of (a) Zr, Nb, Fe, and Zr+Nb; and (b) Cr and Sn, over interfaces of α-Zr and intermetallic and precipitates of P1, P2, and P3. Datasets were collected by the Invizo 6000. The shaded regions around the lines represent uncertainties.

Table 5
Differences in formation energy of $(Zr,Nb)_3Fe$ phase, with composition of $Zr_{76}Nb_{68}Fe_{48}$, for three scenarios of Nb partitioning in the two Zr sublattices of 4c and 8f, using the Wyckoff nomenclature.

	Nb partitioning		ΔE at ground state (meV/f.u.)	$\Delta E\text{-}T\Delta S^{max}$ at 400 °C (meV/f.u.)
	4c site	8f site		
Case 1	0	100 %	0	0
Case 2	50 %	50 %	+99	+83
Case 3	70.6 %	29.4 %	+109	+113

The match to $(Zr,Nb)_3Fe$ stoichiometry is extremely good for P1 and P3, but the Fe content of P2 phase is ~ 6 % higher than the value of (Zr+Nb)/3 for this particle. It is not known whether this indicates that the phase can deviate from stoichiometry, or whether there is some error in the measured composition of P2. Cylindrical ROIs were positioned normal to each matrix/precipitate interface for all three particles and the Zr, Nb, Fe, Cr and Sn composition profiles are shown in Fig. 8. Fe and Nb contents increase from the matrix to precipitates and remain constant within the precipitate for P1 and P3, while these concentrations vary within the P2 precipitate. Although we cannot rule out measurement errors, they are unlikely to lead to such fluctuations between the elemental species observed. There are no overlapping peaks with Fe in the atom probe mass spectrum that would be expected to lead to overestimation of its composition. A physical explanation for this observation is that these precipitates are stable in a range of compositions, with either (Zr,Nb)-site sub-stoichiometry, or with excess Fe on the (Zr,Nb) positions of the structure. Similar fluctuation of the chemistry in SPPs and co-precipitation of $Zr_3(Fe,Cu)$ and $Zr(Nb,Fe,Cr)_2$ is reported in a previous study [49].

Like for the β-Nb precipitates, the concentration of Sn in the precipitate is much lower than the matrix. Slight segregation of Sn at the interface of precipitates is also visible in Fig. 7. Mn, V and Ti are residual elements and appear at higher concentrations in the precipitates than the matrix (detailed in Table S1 of the Supporting Information).

To provide greater confidence in our interpretation of the APT data, we performed DFT simulations to calculate the energy associated with various crystal structures that have a chemical composition close to that reported in Table 3. Zr_3Fe contains two Zr positions at Wyckoff sites *4c* and *8f,* so the preferred accommodation site for Nb needs to be resolved first. At the composition reported in Table 3, Nb could be accommodated in either, or both of the sites. We assumed three bounding cases, summarised in Table 5.

The *4c* sublattice comprises only 25 % of all sites in the crystal structure, while there are ~35 % Nb atoms, thus it is impossible to accommodate all Nb atoms in the *4c* sublattice without spilling over into the *8f* sublattice. Nb preferentially occupies the *8f* site, with a significant enthalpy gain of 99–109 meV per formula unit (f.u.) compared to the cases 2 and 3 where some of the Nb occupies the *4c* sublattice. If this trend was conserved for a higher Nb content of 50 at. %, then it would effectively form an ordered $ZrNb_2Fe$ structure. Including the configurational entropy contribution to the free energy would favour the most disordered case (case 2), but the contribution appears to be small: as an upper bound estimate, the maximal configurational entropy difference (which assumes regular solution) at a representative annealing temperature of 400 °C, is only –16 meV/f.u.

A direct comparison between the $Zr(Nb,Fe)_2$ and $(Zr,Nb)_3Fe$ structure can only occur when the composition (in at %) is exactly 33.33Zr-41.67Nb-25Fe. At this composition, the reaction is in favour of the Laves phase $Zr(Nb,Fe)_2$, suggesting that ternary Zr-Nb-Fe phases with 33 at % Zr are most likely Laves phases.

$$(Zr,Nb)_3Fe \rightarrow Zr(Nb,Fe)_2 \quad \Delta E_1 = \ \& - 41 \text{ meV/f.u.} \tag{4}$$

However, this is at a much lower Zr content than that measured in this work. When the Zr content is above 33 at. %, excess Zr in the Laves

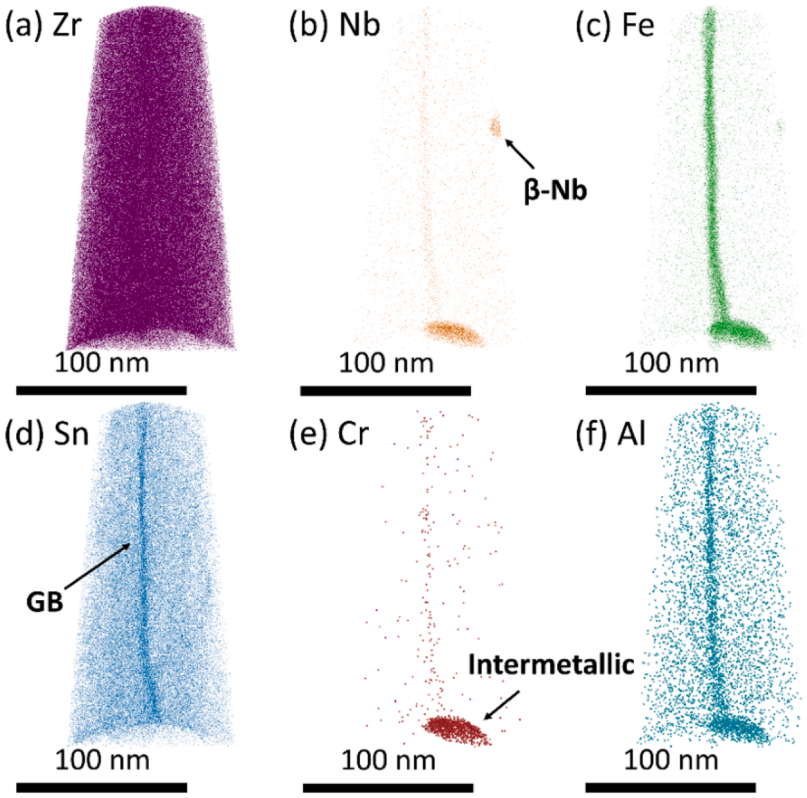

Fig. 9. Reconstructed positions of (a) Zr, (b) Nb, (c) Fe, (d) Sn, (e) Cr, and (f) Al for a dataset containing a grain boundary (GB3) and an intermetallic phase, labelled P4 in this study. This data was obtained from LEAP 4000X Si. Cr, and Al are rendered with 1 nm spheres to enhance visibility. Black arrows indicate GB, intermetallic and β-Nb phases.

Table 6
Bulk concentration analysis of elements in the intermetallic phase in Fig. 9. The number in brackets represents the uncertainty in the least significant digit, e.g. 40.60(8) = 40.60 ± 0.08 at. %.

	Zr	Nb	Fe	Sn	Al	Cr	Si
P4	65.7(5)	10.5(2)	20.2(2)	0.51(3)	1.13(4)	1.97(7)	0.007(4)

phase must be accommodated in the Nb-Fe sublattice, forming a $Zr(Zr,Nb,Fe)_2$ phase. Calculations with the composition of 39.6 % Zr, 35.4 % Nb and 25 % Fe, indicate that the reverse reaction is preferable, confirming that $(Zr,Nb)_3Fe$ is more favourable than a Laves phase with excess Zr.

$$(Zr,Nb)_3Fe \rightarrow Zr(Zr,Nb,Fe)_2 \quad \Delta E_2 = \ \& + 92 \text{ meV/f.u.} \tag{5}$$

The optimised $(Zr,Nb)_3Fe$ structure is included in the Supporting Information, Table S2 and Figure S10. Finally, to assess the thermodynamic stability of $(Zr,Nb)_3Fe$ at the measured compositions, we considered the decomposition energy from the high-temperature stable phase of $(Zr,Nb)_2Fe$. A $(Zr,Nb)_2Fe$ phase with the same Nb content was created, with equation balanced with α-Zr, approximated here as pure hcp-Zr:

$$(Zr,Nb)_3Fe \rightarrow \alpha - Zr + (Zr,Nb)_2Fe \quad \Delta E_3 = \ + 35 \text{ meV/f.u.} \tag{6}$$

This suggests a small energy preference for the formation of the $(Zr,Nb)_3Fe$ over $(Zr,Nb)_2Fe$. Comparing this to the binary Zr-Fe system (equation 7),

$$Zr_3Fe \rightarrow \alpha - Zr + Zr_2Fe \quad \Delta E_4 = \ + 45 \text{ meV/f.u.} \tag{7}$$

suggests that the addition of Nb reduces the thermodynamic driving force for the formation of the Zr_3Fe-type intermetallic phase. In both cases, the energies of formation are negative suggesting that the Zr_3Fe-type intermetallic is likely to be preferable over the Zr_2Fe-type phase, even when Nb is added to the intermetallic phases. However, the reaction energies presented here, with the exception of Eq. (5), are small enough that the effects of temperature, strain, and interfacial energy that are not explicitly included in these calculations may alter the current findings.

Electronic and magnetic entropy contributions are likely to be comparable amongst all phases considered here, thus their contributions to the free energy of reactions (4–7) is most likely negligible[50]. Conversely, configurational and vibrational entropy contributions may be significant, especially at annealing temperatures [50]. These could be calculated accurately using ensemble statistics methods and quasi-harmonic of fully anharmonic approximations, respectively. However, considering the size of the precipitates, we are cautious against doing it without accounting for the interfacial energy between the SPP and the matrix and any resulting residual stresses from cooling, as these are likely to dominate the second-order effects. Interfacial and strain energies are particularly important if interface is found to be coherent or semi-coherent. Unfortunately, little is known about the interface or even the preferred crystallographic orientation relationship between the SPPs and the α-Zr matrix, and thus the interfacial energy of the system cannot be reliably estimated. Adding the entropic contribution alone may provide a misleading refinement of the current results, which are to be treated as a first order approximation.

Nevertheless, when combining the APT stoichiometry analysis performed on the precipitates, with the reasonably large positive value of Eq. (5) that confirms the unlikely accommodation of excess Zr on the Fe sublattice of $Zr(Nb,Fe)_2$, there is reasonable evidence that the phase of precipitates P1-P3 are most likely $(Zr,Nb)_3Fe$. The small but positive decomposition enthalpies at ground state (Eq (6)–7), while not definitive, provide further confidence in support of this argument.

Fig. 9 is an APT dataset showing Zr, Fe, Nb and Sn atoms at a grain boundary (GB3), which is connected to an intermetallic phase (P4) at the base of the tip, acquired right before the specimen fractured. This data was collected by using a LEAP 4000 X Si. An isosurface of 10 at. % (Nb, Fe) was used to define the surface of this very thin intermetallic. The proxigram, normal to the interface of precipitates with α-Zr is presented in Figure S6 of the Supporting Information. The results are shown in Table 6. The precipitate forms mostly from Zr, Fe and Nb, resembling the composition of C15, cubic $(Zr,Nb)_2Fe$ Laves phase with its characteristically low Nb content (~10 % Nb, ~30 % Fe, ~60 %Zr) [21]. It is believed that Nb replaces Zr in Zr_2Fe to form this Laves phase. Although Zr_2Fe is stable at high temperatures (>775°C), $(Zr,Nb)_2Fe$ Laves phase is frequently observed [21] in Zr alloys due to the nonequilibrium conditions during the manufacturing of Zr alloys. Residual Cr and Al have segregated to this Laves phase. It is worth noting that this particle is very thin and in contact with a grain boundary (GB3), providing fast diffusion pathway for alloying elements, therefore, it is impossible to unambiguously identify this precipitate as a $(Zr,Nb)_2Fe$ Laves phase. Another small β-Nb phase is captured on the right side of this sample (Fig. 9), but the composition of this particle is not considered in this study due to its very small size. However, there is a thin shell of Fe around this particle, similar to larger the β-Nb particles discussed in the previous section.

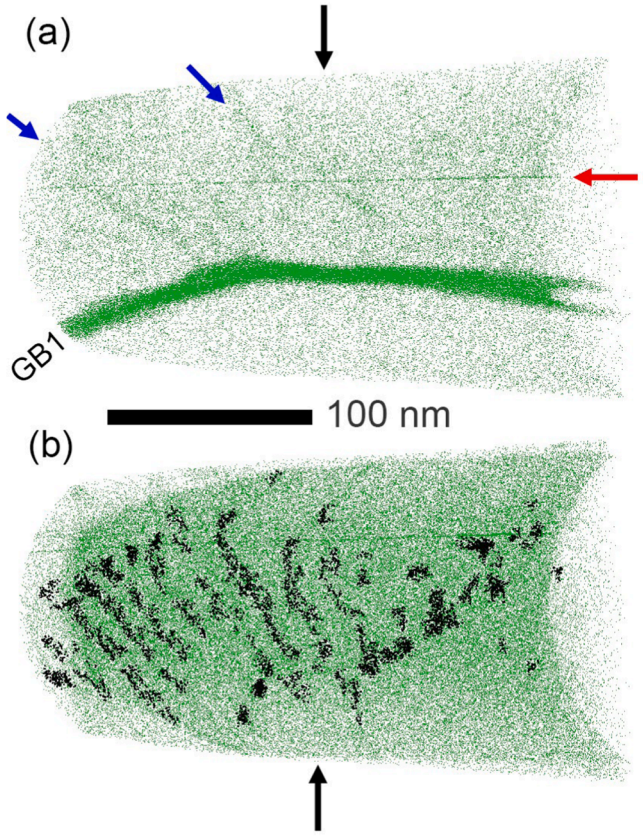

Fig. 10. Reconstructed position n of (a) Fe atoms, presenting the grain boundary GB1 and low angle grain boundary protruding from the high angle boundary; (b) top view of Fe atom positions, with black spots indicating clusters of Fe atoms separate from the grain boundary. The black arrow in (a) indicates the view shown in (b), and visa versa. The blue arrows indicate the angle of the low angle grain boundaries. The red arrow indicates a "hot" pixel resulting from contamination in the multichannel plate during acquisition. This hot pixel was completely excluded from all microanalysis.

3.4. Grain boundaries

In total, 3 grain boundaries were detected in our samples, labelled GB1 to GB3. The dataset in Fig. 9 contains one of these grain boundaries (GB3); GB1 is presented in Fig. 10 and GB2 is shown in Figure S7 of the

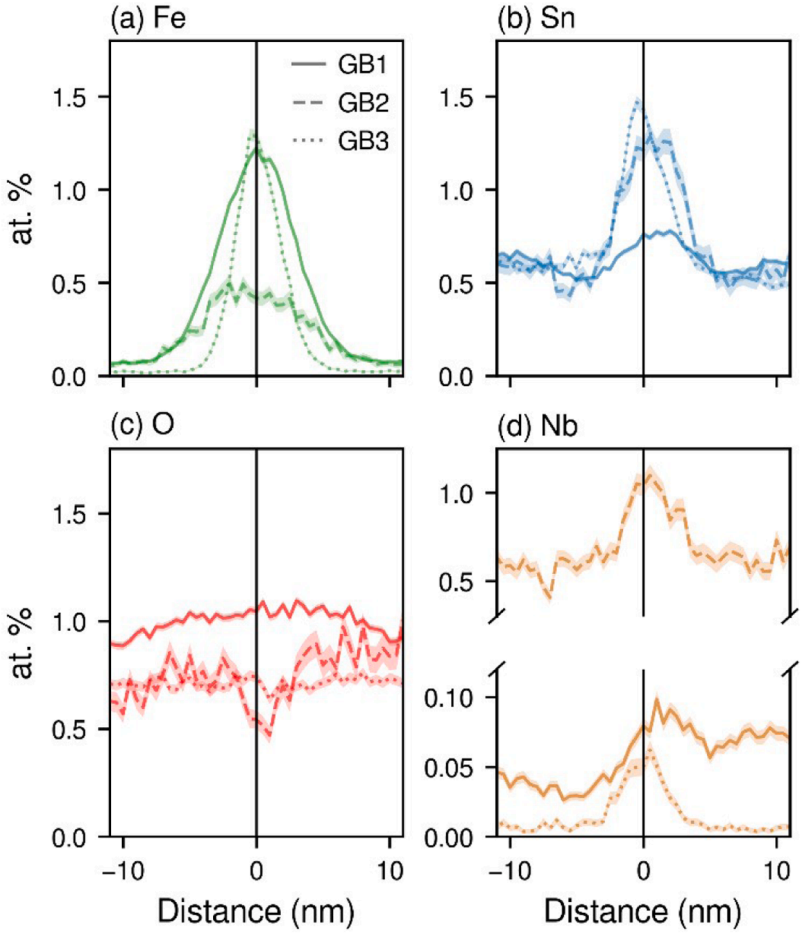

Fig. 11. Composition profiles over grain boundaries. GB1and GB2 were collected on the Invizo 6000, whereas GB3 was collected on the LEAP4000 X Si. Note the split vertical axis on (d).

Supporting Information. In each case, the reconstructed volume has been oriented such that the planar feature (the grain boundary) is edge on, appearing as a line spanning the image. Each GB specimen was prepared by site-specific FIB annular milling. All solute metals, including Sn, exhibit some degree of segregation to the grain boundary.

Fig. 10 shows reconstructed position of Fe in a large dataset obtained using the Invizo 6000. This specimen contains interesting structures, including a grain boundary heavily decorated with Fe. The TKD data (Fig. 1) shows that these samples contain a high density of low angle grain boundaries. Roughly one-third-of the way down the tip, we see a planar feature protruding from the boundary to which some Fe has segregated. This is thought to be a low angle grain boundary connected to a high angle grain boundary. The low angle boundary consists of an array of dislocations and attracts less segregation than the high angle boundary. This distribution is demonstrated by black dots in Fig. 10(b) on the top view of the grain boundary. These black Fe positions were identified using cluster analysis. The distribution of Fe in the upper grain is also inhomogeneous, but away from the interfaces. This is thought to be segregation of the Fe to dislocations (i.e. Cottrell atmospheres [51]).

ROIs were created normal to the grain boundaries to calculate a 1D compositional profile of Fe, Nb, Sn, and O across all three grain boundaries, as shown in Fig. 11. Fe is nearly absent in the α-Zr but rises to ~ 1.2 at. % at two of the boundaries (GB1 and GB3). Similarly, the concentration of Sn is ~0.53 at. % in the matrix and ~1.3 at. % at GB2. Although Nb segregates in all samples, the concentrations at both the matrix and grain boundary vary significantly between samples, specifically for GB2. This might be due to the proximity of the grain boundary to β-Nb precipitates and/or intermetallic phases; The position of RIO for GB2 is presented in Figure S8 of the Supporting Information, demonstrating its close proximity to an intermetallic phase. O is detected in the form of ZrO^{+}, ZrO^{++} and O^{+}, like previous studies [38,52]. The proportion of decomposed O content is around 0.69 at. % in the matrix and reaches ~1.2 at. % at the grain boundary in GB1, but falls to ~0.5 at. % in GB2. The large variability of segregated elements between grain boundaries is thought to be due to a combination of the type of the boundary, and the proximity of other features, such as precipitates, that draw certain atomic species via grain boundary diffusion.

Like for the precipitate interfaces, artefacts due to local magnification effects in APT [25] can hinder the ability to achieve high spatial

Table 7
The Gibbsian interfacial excess and fractional monolayer coverage of Fe, Nb, and Sn for the three grain boundaries described in this work. All interfacial excess measurements were made using 1D concentration profiles along cylindrical ROIs. The uncertainty is propagated from the uncertainty in the Fe measurement [26].

	GB1	GB2	GB3
N_{Fe} (atoms)	41,946 ± 1672	1993 ± 376	13,713 ± 591
Γ_{Fe} (atoms/nm^{-2})	4.2 ± 0.2	1.8 ± 0.3	3.4 ± 0.2
ϕ_{Fe} (fractional monolayer)	0.31 ± 0.01	0.13 ± 0.03	0.25 ± 0.01
N_{Nb} (atoms)	447 ± 669	1315 ± 656	513 ± 172
Γ_{Nb} (atoms/nm^{-2})	0.05 ± 0.07	1.2 ± 0.6	0.13 ± 0.04
ϕ_{Nb} (fractional monolayer)	0.003 ± 0.005	0.08 ± 0.04	0.009 ± 0.003
N_{Sn} (atoms)	2287 ± 2373	1365 ± 616	8341 ± 1249
Γ_{Sn} (atoms/nm^{-2})	0.2 ± 0.2	1.2 ± 0.6	2.1 ± 0.3
ϕ_{Sn} (fractional monolayer)	0.02 ± 0.02	0.09 ± 0.04	0.15 ± 0.02

resolution when mapping the distribution of solute grain boundaries [38]. The segregated layer at the grain boundary shown in Fig. 11 might appear thicker than the original material due to trajectory aberrations that arise from the varying geometry of the specimen during field evaporation [25]. Therefore, it is likely that the maximum values shown in this figure are lower than their concentrations at the boundary. The interfacial concentration of Fe, Sn, and Nb are calculated using the method described in section 3.2, summarised in Table 7.

The main finding from these results is that Fe segregates the most strongly of the solutes at these boundaries, relative to the matrix composition. The very low solubility of Fe in the α-Zr matrix provides a driving force for segregation.

Solute segregation to grain boundaries affects the mechanical properties and corrosion resistance of Zr alloys [39], influencing stress corrosion cracking [53], thermal stability, and hydrogen embrittlement [54] through intergranular mechanisms [55]. Sn segregation to grain boundaries generally causes a reduction in both tensile strength [56,57] and corrosion resistance [57]. Previous studies [22,35] demonstrated that Fe segregation to grain boundaries does not promote stress-induced corrosion in Zr alloys and could improve the corrosion resistance compared to Zr alloys with supersaturated solid solution within the matrix [38]. Both Fe and Nb are suggested to have strengthening effect on the grain boundaries, with Fe having a greater effect [55,56].

4. Conclusion

Atomic scale compositional information is provided for different microstructural features in Optimised ZIRLO. This includes β-Nb, Zr-Nb-Fe intermetallic phases and solute distribution in the Zr matrix, SPPs, and grain boundaries. This Zr alloy contains β-Nb second phase with over 80 at. % Nb and ~15 at. % Zr, which were decorated by Fe atoms with <1 nm thickness and varied concentrations of 0.5 to 1.2 at. %.

Compositional analysis of Zr-Nb-Fe intermetallic phases with ~39 at. % Nb, revealed a much better compositional match for $(Zr,Nb)_3Fe$ and a poor match for C14 $Zr(Nb,Fe)_2$. DFT calculations further support that at the measured composition, the $Zr(Nb,Fe)_2$ Laves phase is thermodynamically unstable at the ground state and there is an enthalpic driving force to form $(Zr,Nb)_3Fe$ intermetallic phase. This driving force is small enough that contributions from interfacial energy and residual strain and, at elevated temperatures, also from vibrational and configurational entropy, may alter the ground state thermodynamics. Interestingly, it is expected that the Nb would only occupy one of the two Zr sub-lattices in the crystal structure of $(Zr,Nb)_3Fe$. Our findings supports the debate that hexagonal $(Zr,Nb)_3Fe$ has been misidentified as $Zr(Nb,Fe)_2$ in the literature for Zr-Fe-Nb alloys.

Compositional analysis along the grain boundary has revealed the segregation of Fe, Sn, Nb, and Cr. Of these, Fe, Nb, and Cr segregation is known to enhance the strength of the alloy. The segregation of elements at the grain boundary are also likely to influence corrosion resistance and these results will be useful for future corrosion studies. No Sn segregation was observed near the interface of β-Nb with the α-Zr matrix, while a slight Sn segregation was detected at the interface of the intermetallic phases with the α-Zr and at the grain boundaries.

CRediT authorship contribution statement

Siyu Huang: Writing – original draft, Methodology, Investigation, Data curation. **Levi Tegg:** Visualization, Validation, Supervision, Formal analysis, Data curation. **Sima Aminorroaya Yamini:** Writing – review & editing, Validation, Project administration, Conceptualization. **Lucia Chen:** Writing – review & editing, Software. **Patrick Burr:** Writing – review & editing, Supervision, Software, Resources, Formal analysis. **Jiangtao Qu:** Methodology, Data curation. **Limei Yang:** Methodology, Data curation. **Ingrid McCarroll:** Supervision. **Julie M. Cairney:** Writing – review & editing, Validation, Supervision, Resources, Funding acquisition, Conceptualization.

Declaration of competing interest

The authors declare that they have no known competing financial interests or personal relationships that could have appeared to influence the work reported in this paper.

Acknowledgements

All authors acknowledge the technical and scientific assistance of Sydney Microscopy & Microanalysis, the University of Sydney node of Microscopy Australia. Lucia Chen acknowledges the Tyree foundation for financial support through a philanthropic Tyree UNSW nuclear engineering scholarship.

Supplementary materials

Supplementary material associated with this article can be found, in the online version, at doi:10.1016/j.actamat.2025.121365.

References

[1] G. Yuan, G. Cao, Q. Yue, L. Yang, Y. Yun, G. Shao, J. Hu, Formation and fine-structures of nano-precipitates in ZIRLO, J. Alloys Compd. 687 (2016) 451–457.
[2] J.P. Foster, H.K. Yueh, R.J. Comstock, ZIRLOTM cladding improvement, J. ASTM Int. 5 (2008) 1–13.
[3] A. Fazi, K. Stiller, H.-O. Andrén, M. Thuvander, Cold sprayed Cr-coating on Optimized ZIRLO™ claddings: the Cr/Zr interface and its microstructural and chemical evolution after autoclave corrosion testing, J. Nucl. Mater. 560 (2022) 153505.
[4] Y. Matsukawa, H. Yang, K. Saito, Y. Murakami, T. Maruyama, T. Iwai, K. Murakami, Y. Shinohara, T. Kido, T. Toyama, The effect of crystallographic mismatch on the obstacle strength of second phase precipitate particles in dispersion strengthening: bcc Nb particles and nanometric Nb clusters embedded in hcp Zr, Acta Mater 102 (2016) 323–332.
[5] Y. Matsukawa, I. Okuma, H. Muta, Y. Shinohara, R. Suzue, H. Yang, T. Maruyama, T. Toyama, J. Shen, Y. Li, Crystallographic analysis on atomic-plane parallelisms between bcc precipitates and hcp matrix in recrystallized Zr-2.5 Nb alloys, Acta Mater 126 (2017) 86–101.
[6] Y. Matsukawa, S. Kitayama, K. Murakami, Y. Shinohara, K. Yoshida, H. Maeno, H. Yang, T. Toyama, K. Yasuda, H. Watanabe, Reassessment of oxidation-induced amorphization and dissolution of Nb precipitates in Zr− Nb nuclear fuel cladding tubes, Acta Mater 127 (2017) 153–164.
[7] Y.H. Jeong, H.G. Kim, T.H. Kim, Effect of β phase, precipitate and Nb-concentration in matrix on corrosion and oxide characteristics of Zr–xNb alloys, J. Nucl. Mater. 317 (2003) 1–12.
[8] R. Kondo, N. Nomura, Y. Tsutsumi, H. Doi, T. Hanawa, Microstructure and mechanical properties of as-cast Zr–Nb alloys, Acta Biomater 7 (2011) 4278–4284.
[9] N. Nomura, Y. Tanaka, R. Kondo, H. Doi, Y. Tsutsumi, T. Hanawa, Effects of phase constitution of Zr-Nb alloys on their magnetic susceptibilities, Mater. Trans. 50 (2009) 2466–2472.
[10] J. Wei, P. Frankel, E. Polatidis, M. Blat, A. Ambard, R. Comstock, L. Hallstadius, D. Hudson, G. Smith, C. Grovenor, The effect of Sn on autoclave corrosion performance and corrosion mechanisms in Zr–Sn–Nb alloys, Acta Mater 61 (2013) 4200–4214.
[11] C. Toffolon-Masclet, J. Brachet, C. Servant, J. Joubert, P. Barberis, N. Dupin, P. Zeller, Contribution of thermodynamic calculations to metallurgical studies of multi-component zirconium based alloys, J. ASTM Int. 5 (2008) JAI101122.
[12] A. Aldeen, Z. Chen, I. Disher, M. Samiuddin, K. Yan, Second phase particles in Zr–Sn–Nb–Fe alloys: a review, Phys. Met. Metallogr. 124 (2023) 362–379.
[13] A.T. Motta, A. Couet, R.J. Comstock, Corrosion of zirconium alloys used for nuclear fuel cladding, Annu Rev Mater Res 45 (2015) 311–343.
[14] A. Couet, A.T. Motta, A. Ambard, D. Livigni, In-situ electrochemical impedance spectroscopy measurements of zirconium alloy oxide conductivity: relationship to hydrogen pickup, Corros. Sci. 119 (2017) 1–13.
[15] P. Rudling, G. Wikmark, A unified model of Zircaloy BWR corrosion and hydriding mechanisms, J. Nucl. Mater. 265 (1999) 44–59.
[16] Z. Yu, E. Kautz, T. Kim, S. Lambeets, A. Devaraj, A. Couet, Chemical redistribution of alloying elements in growing oxides formed on irradiated Zr-Nb-Fe alloys and its implication on corrosion, in: S.K. Yagnik, M. Preuss (Eds.), Zirconium in the Nuclear Industry: 20th International Symposium, ASTM International, 2023, p. 0.
[17] M. Granovsky, M. Canay, E. Lena, D. Arias, Experimental investigation of the Zr corner of the ternary Zr–Nb–Fe phase diagram, J. Nucl. Mater. 302 (2002) 1–8.
[18] H.-G. Kim, J.-Y. Park, Y.-H. Jeong, Ex-reactor corrosion and oxide characteristics of Zr–Nb–Fe alloys with the Nb/Fe ratio, J. Nucl. Mater. 345 (2005) 1–10.
[19] C. Ramos, C. Saragovi, M. Granovsky, Some new experimental results on the Zr–Nb–Fe system, J. Nucl. Mater. 366 (2007) 198–205.
[20] F. Stein, G. Sauthoff, M. Palm, Experimental determination of intermetallic phases, phase equilibria, and invariant reaction temperatures in the Fe-Zr system, J. Ph. Equilibria 23 (2002) 480–494.

[21] A. Harte, M. Griffiths, M. Preuss, The characterisation of second phases in the Zr-Nb and Zr-Nb-Sn-Fe alloys: a critical review, J. Nucl. Mater. 505 (2018) 227–239.
[22] B. Cox, Some thoughts on the mechanisms of in-reactor corrosion of zirconium alloys, J. Nucl. Mater. 336 (2005) 331–368.
[23] V.N. Shishov, M.M. Peregud, A.V. Nikulina, V.F. Kon'kov, V.V. Novikov, V. A. Markelov, T.N. Khokhunova, G.P. Kobylyansky, A.E. Novoselov, Z.E. Ostrovsky, A.V. Obukhov, Structure-phase State, corrosion and irradiation properties of Zr-Nb-Fe-Sn system alloys, J. ASTM Int. 5 (2008) 1–18.
[24] S. Averin, V. Panchenko, A. Kozlov, L. Sinelnikov, V. Shishov, A. Nikulina, G. Sabol, G. Moan, Evolution of dislocation and precipitate structure in Zr alloys under long-term irradiation, in: Zirconium in the Nuclear Industry: Twelfth International Symposium, ASTM International, 2000, pp. 105–121.
[25] B. Gault, M.P. Moody, J.M. Cairney, S.P. Ringer, Atom Probe Microscopy, Springer, 2012. Kindle Edition ed.
[26] L. Tegg, J.M. Cairney, Uncertainties in interfacial excess calculations from atom probe tomography data, J Microsc 298 (2025) 262–273.
[27] D. Tomus, H.P. Ng, In situ lift-out dedicated techniques using FIB–SEM system for TEM specimen preparation, Micron 44 (2013) 115–119.
[28] A. van de Walle, P. Tiwary, M. de Jong, D.L. Olmsted, M. Asta, A. Dick, D. Shin, Y. Wang, L.Q. Chen, Z.K. Liu, Efficient stochastic generation of special quasirandom structures, Calphad 42 (2013) 13–18.
[29] G. Kresse, J. Furthmüller, Efficient iterative schemes for ab initio total-energy calculations using a plane-wave basis set, Physical Review B 54 (1996) 11169–11186.
[30] S. Hanlon, S. Persaud, F. Long, A. Korinek, M. Daymond, A solution to FIB induced artefact hydrides in Zr alloys, J. Nucl. Mater. 515 (2019) 122–134.
[31] M.A. Tunes, C.M. Silva, P.D. Edmondson, Site specific dependencies of hydrogen concentrations in zirconium hydrides, Scripta Mater 158 (2019) 136–140.
[32] H. Tian, X. Wang, W. Gong, J. Zhou, H. Zhang, Recrystallization behavior of cold-rolled Zr–1Nb alloy, J. Nucl. Mater. 456 (2015) 321–328.
[33] O.T. Woo, M. Griffiths, The role of Fe on the solubility of Nb in α-Zr, J. Nucl. Mater. 384 (2009) 77–80.
[34] P. Lei, G. Ran, C. Liu, C. Ye, D. Lv, J. Lin, Y. Wu, J. Xu, In situ TEM study of microstructure evolution of Zr-Nb-Fe alloy irradiated by 800 keV Kr(2+) ions, Materials (Basel) 10 (2017).
[35] Z. Yu, M. Bachhav, F. Teng, L. He, M. Dubey, A. Couet, STEM/EDS and APT study on the microstructure and microchemistry of neutron irradiated ZIRLOTM, J. Nucl. Mater. 573 (2023) 154139.
[36] E. Francis, A. Harte, P. Frankel, S. Haigh, D. Jädernäs, J. Romero, L. Hallstadius, M. Preuss, Iron redistribution in a zirconium alloy after neutron and proton irradiation studied by energy-dispersive X-ray spectroscopy (EDX) using an aberration-corrected (scanning) transmission electron microscope, J. Nucl. Mater. 454 (2014) 387–397.
[37] L. Tegg, A.J. Breen, S. Huang, T. Sato, S.P. Ringer, J.M. Cairney, Characterising the performance of an ultrawide field-of-view 3D atom probe, Ultramicroscopy 253 (2023) 113826.
[38] D. Hudson, G.D. Smith, Initial observation of grain boundary solute segregation in a zirconium alloy (ZIRLO) by three-dimensional atom probe, Scripta Mater 61 (2009) 411–414.
[39] M.K. Miller, R.G. Forbes, M.K. Miller, R.G. Forbes, Introduction to atom-probe tomography, Atom-Probe Tomography Local Electrode Atom Probe (2014) 1–49.
[40] S. Huang, L. Tegg, J. Qu, L. Yang, I. McCarroll, P. Burr, J.M. Cairney, Nanoscale distribution of alloying elements in optimized ZIRLO using the Invizo 6000, Microsc. Microanal. 29 (2023) 614–615.
[41] G. Sundell, M. Thuvander, P. Tejland, M. Dahlbäck, L. Hallstadius, H.O. Andrén, Redistribution of alloying elements in Zircaloy-2 after in-reactor exposure, J. Nucl. Mater. 454 (2014) 178–185.
[42] Y. Chen, Z. Liu, D. Wang, Y. Zhao, First-principles study of oxygen in ω-Zr, Metals (Basel) 13 (2023) 1042.
[43] T.B. Massalski, H. Okamoto, P. Subramanian, L. Kacprzak, W.W. Scott, Binary Alloy Phase Diagrams, American society for metals Metals Park, OH, 1986.
[44] S. Huang, L. Tegg, S. Aminorroaya Yamini, Z. Wang, Y. Huang, L. Yang, O. Muránsky, I. McCarroll, P.A. Burr, J.M. Cairney, Grain refinement and solute distribution in Zircaloy-4 following high-pressure torsion, J. Mater. Eng. Perform. (2025).
[45] S. Hofmann, P. Leiĉek, Solute segregation at grain boundaries, Interface Sci. 3 (1996) 241–267.
[46] B. Gault, P.J. Felfer, M. Ivermark, H. Bergqvist, J.M. Cairney, S.P. Ringer, Atom probe microscopy characterization of as quenched Zr–0.8wt% Fe and Zr–0.15wt% Cr binary alloys, Mater. Lett. 91 (2013) 63–66.
[47] P.A. Burr, M.R. Wenman, B. Gault, M.P. Moody, M. Ivermark, M.J.D. Rushton, M. Preuss, L. Edwards, R.W. Grimes, From solid solution to cluster formation of Fe and Cr in α-Zr, J. Nucl. Mater. 467 (2015) 320–331.
[48] F. Stein, M. Palm, G. Sauthoff, Structure and stability of Laves phases. Part I. Critical assessment of factors controlling Laves phase stability, Intermetallics 12 (2004) 713–720.
[49] B. Tao, B. Luan, R. Qiu, Q. Fang, L. Cao, Y. Liu, X. Zhang, R. Liu, Q. Liu, Analysis of atomic distribution near grain boundary in ZrSnNbFe-(Cu) alloys by atom probe tomography, J. Nucl. Mater. 515 (2019) 135–139.
[50] V. Tuli, P. Burr, A. Claisse, C. Cazorla, Thermodynamic stability of β-phases in Zr-Nb alloys, Phys. Rev. Mater. 7 (2023) 113607.
[51] G.D.W. Smith, D. Hudson, P.D. Styman, C.A. Williams, Studies of dislocations by field ion microscopy and atom probe tomography, Philos. Mag. 93 (2013) 3726–3740.
[52] Y. Dong, A.T. Motta, E.A. Marquis, Atom probe tomography study of alloying element distributions in Zr alloys and their oxides, J. Nucl. Mater. 442 (2013) 270–281.
[53] A. King, G. Johnson, D. Engelberg, W. Ludwig, J. Marrow, Observations of intergranular stress corrosion cracking in a grain-mapped polycrystal, Science 321 (2008) 382–385.
[54] H.C. Rogers, Hydrogen embrittlement of metals: atomic hydrogen from a variety of sources reduces the ductility of many metals, Science 159 (1968) 1057–1064.
[55] Z. Xue, X. Zhang, J. Qin, M. Ma, R. Liu, Exploring the effects of solute segregation on the strength of Zr $\{10\bar{1}1\}$ grain boundary: a first-principles study, J. Alloys Compd. 812 (2020) 152153.
[56] M. Christensen, T. Angeliu, J. Ballard, J. Vollmer, R. Najafabadi, E. Wimmer, Effect of impurity and alloying elements on Zr grain boundary strength from first-principles computations, J. Nucl. Mater. 404 (2010) 121–127.
[57] R. Yuan, Y.-P. Xie, T. Li, C.-H. Xu, M.-Y. Yao, J.-X. Xu, H.-B. Guo, B.-X. Zhou, An origin of corrosion resistance changes of Zr alloys: effects of Sn and Nb on grain boundary strength of surface oxide, Acta Mater 209 (2021) 116804.